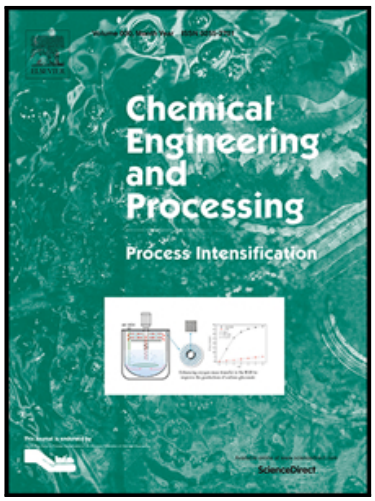

Intensification of liquid mixing and local turbulence using a fractal injector with staggered conformation

Shuxian Jiang , Marc-Olivier Coppens , Jiajun Wang

PII: S0255-2701(22)00252-5
DOI: https://doi.org/10.1016/j.cep.2022.109042
Reference: CEP 109042

To appear in: *Chemical Engineering and Processing - Process Intensification*

Received date: 27 March 2022
Revised date: 11 June 2022
Accepted date: 30 June 2022

Please cite this article as: Shuxian Jiang , Marc-Olivier Coppens , Jiajun Wang , Intensification of liquid mixing and local turbulence using a fractal injector with staggered conformation, *Chemical Engineering and Processing - Process Intensification* (2022), doi: https://doi.org/10.1016/j.cep.2022.109042

Highlights

- Intensification of liquid-liquid processes using a fractal injector is studied
- Conformation effects on injector performance without changing fractal dimension
- CFD simulations use 3D unsteady RANS with finite-rate/eddy dissipation (FR/EDM)
- The FR/EDM is modified for fast liquid-liquid reactions with local micromixing
- Local turbulence and micromixing are intensified using a staggered conformation

Intensification of liquid mixing and local turbulence using a fractal injector with staggered conformation

Shuxian Jiang[a], Marc-Olivier Coppens[a,*], Jiajun Wang[b,*]

[a]Centre for Nature Inspired Engineering & Department of Chemical Engineering, University College London, Torrington Place, London, UK

[b]State Key Laboratory of Chemical Engineering, College of Chemical and Biological Engineering, Zhejiang University, Hangzhou, PR China

*Correspondence

Email addresses: m.coppens@ucl.ac.uk (Marc-Olivier Coppens), jiajunwang@zju.edu.cn (Jiajun Wang).

Abstract

Two self-similar, tree-like injectors of the same fractal dimension are compared, demonstrating that other geometric parameters besides dimension play a crucial role in determining mixing performance. In one injector, when viewed from the top, the conformation of branches is eclipsed; in the other one, it is staggered. The flow field and the

fractal injector induced mixing performance are investigated through computational fluid dynamics (CFD) simulations. The finite rate/eddy dissipation model (FR/EDM) is modified for fast liquid-phase reactions involving local micromixing. Under the same operating conditions, flow field uniformity and micromixing are improved when a staggered fractal injector is used. This is because of enhanced jet entrainment and local turbulence around the spatially distributed nozzles. Compared with a traditional double-ring sparger, a larger reaction region volume and lower micromixing time are obtained with fractal injectors. Local turbulence around the spatially distributed nozzles in fractal injectors improves reaction efficiency.

Keywords

fractal, turbulence, mixing, computational fluid dynamics (CFD); process intensification; multiphase reactions

Nomenclature

b	scaling ratio
C_i	molecular concentration of species i in the reaction region, kmol/m^3
C_{iE}	averaged molecular concentration of species i in the ambient fluid, kmol/m^3
$C_{j,r}$	molar concentration of species, kmol/m^3
e_1, e_2	length of horizontal tubes in parent and child generations, mm
d	diameter of nozzles, mm
d_1, d_2	diameter of tubes in parent and child generations, mm
D	fractal dimension
D_m	molecular diffusivity, m^2/s
$D_{i,m}$	mass diffusion coefficient of species i, m^2/s
E	engulfment parameter, 1/s
h	mounting height of mixers, mm

H	vessel height, m
I	ionic strength
$\boldsymbol{J_i}$	local diffusion flux of species i, kg/(m^2·s)
$k_{f,r}$, $k_{b,r}$	the forward and backward reaction-rate constant
l_1, l_2	length of the vertical tubes in parent and child generations, mm
M_i	molecular weight of species i, kg/kmol
n_i	molar number of species i in the vessel at time t, kmol
$n_{i,0}$	molar number of species i in the vessel at time t = 0, kmol
$n'_{j,r}$, $n''_{j,r}$	rate exponent for reactant species j and product species j
N_c	number of cells in calculation domain
p	pressure, Pa
Re_j	injection Reynolds number
R_i	production rate of species i by chemical reaction, kg/(m^3·s)
$R_{i,r}$	net source of i in reaction r, kmol/(m^3·s)
$R^r_{i,r}$	intrinsic rate of species i in reaction r, kmol/(m^3·s)
$R^t_{i,r}$	overall source of chemical species i controlled by the turbulent mixing, kmol/(m^3·s)
S	modulus of the mean rate-of-strain tensor, s^{-1}
Sc_t	turbulent Schmidt number
S_i	species source term, kg/(m^3·s)
S_{ij}	strain rate tensor element, s^{-1}
t	flow time, s
t_m	micromixing time, s
T	vessel diameter, m

u_j injection velocity, m/s

U velocity vector, m/s

V micromixed volume, m^3

V_m volume of cell m, m^3

V_{total} total effective volume of the vessel, m^3

w tracer mass fraction

w_{av} volume averaged tracer mass fraction

w_m tracer mass fraction in cell m

X_S segregation index

X_{H2BO3-} conversion rate of reactant $H_2BO_3^-$

Y ratio of the H^+ consumed by reaction (ii) to the total H^+ injected into the system

Y_i local mass fraction of species i

Y_{ST} value of Y in case of complete segregation

x, y, z Cartesian coordinates, m

Greek letters

ε turbulent dissipation rate, m^2/s^3

η the ratio of the turbulent to mean strain time scale

$\nu'_{i,r}$, $\nu''_{i,r}$ the stoichiometric coefficient for reactant i and product i, respectively.

μ fluid viscosity, kg/(m·s)

μ_t turbulent viscosity, kg/(m·s)

ρ fluid density, kg/m^3

σ_w standard deviation of the tracer mass fraction at time t

Ω vorticity, s^{-1}

Subscripts

m	cell *m*
r	reaction *r*
R	reactant
P	product

1. Introduction

Mixing liquids is a common operation in the chemical industry, and it plays a critical role in fast liquid-phase reactions.[1] Especially in rapid reaction processes, such as polymerization, crystallization and certain organic reactions, the contact mode and mixing behavior between reactants can directly or indirectly affect and determine the quality of products.[2] Jet mixers are widely used as an alternative to impellers to induce rapid mixing of liquids.[3] For a jet mixer, the working fluid is injected into a slowly moving or static bulk fluid at a high speed. At the boundary of the jet, a mixing layer is formed, due to the velocity difference between the working fluid and the bulk fluid. Because of this, a jet mixer can realize the mixing of low viscosity liquids in the reactor by entrainment.[4]

Many new ways have been proposed to achieve fast and efficient liquid mixing. Chaotic advection-based micromixers enhance the diffusive fluxes across interfaces and hereby improve mixing efficiency through advection; this is realized by various flow rearrangements, such as zigzag or serpentine channels, or by introducing obstacles.[5, 6] The invention of the coiled flow inverter (CFI) and further contributions by the group of Professor Krishna Nigam, whom we celebrate in this Festschrift, have been key advances in the intensification of liquid-liquid reactions and other processes. By inducing chaotic advection, helical tubes can intensify the liquid mixing and reaction process under laminar flow conditions[7], and Soni et al.[8] proposed a compact design of the symmetrical CFI, which can achieve good radial mixing while maintaining a narrow RTD. Soleymani et al.[9] found that the development of vortices is essential for good liquid mixing performance. Based on

this, they developed a new T-type micromixer for fast liquid mixing processes, with simulation results revealing that the new mixer could lead to much better mixing efficiency than ordinary T-mixers. Wu et al.[10] found that by adding swirling into the jet flow of a multi-orifice-impinging transverse jet mixer, the jet impingement could be intensified, as many small vortices are generated homogeneously, which leads to relatively fast mixing within a few milliseconds. Splitting the mixing path length into a series of sub-streams can increase the contact surface for mixing liquids, Zhang et al.[11] designed an inline 3D showerhead mixer. Its unique structure with multiple channels can effectively blend two reagent streams and provide intensified mixing. CFD results demonstrated that this mixer performed better than two common commercial T-type micromixers. Pre-mixing behavior is also an important factor influencing the fast mixing process, since it is able to affect the environment for both mesomixing and micromixing, Luo et al.[12] demonstrated increasing micromixing efficiency in a novel helical tube reactor with a pre-mixer, due to the effect of the optimized pre-mixing behavior.

In 1999, Coppens proposed a fractal injector that borrowed from the scaling, fractal properties of trees and lungs[13] and applied it to gas-solid fluidized beds.[14-16] A fractal injector contains a stem (inlet) that divides into several branches, which divide repeatedly over several generations, in a self-similar way. One of the key properties of this injector is its fractal dimension, D, which characterizes its space-filling capacity – $D = 2$ corresponding to an area-filling (e.g., planar) injector, and $D = 3$ to a space-filling one. Experimental results for fluidized beds showed that the hydrodynamics became more uniform and the multiphase mixing process was enhanced by introducing a fractal injector.[17, 18] More generally, by introducing such nature-inspired, hierarchical transport networks into chemical process equipment, transfer and reaction rates can be enhanced in a scalable way, which is a likely reason why fractal networks of an optimized scaling range are so prominent in nature.[19]

Over the past years, fractal injectors and distributors have been used to enhance heat transfer, liquid mixing and multiphase reactor performance [20-23] Fractal scaling has prompted the design of a range of novel equipment,[24-27] and we refer to an earlier article for more references on fractal engineering of fluid dynamics.[28]

In recent work[28], we have investigated the use of a fractal injector as a fast liquid jet mixer, without the requirement of external energy input. The effect of the fractal dimension of the injector on the liquid flow field, vortex structure and mixing performance was investigated, comparing three strictly self-similar fractal injectors with $D = \log(4)/\log(2) = 2$, $D = \log(6)/\log(2) = 2.58$ and $D = \log(8)/\log(2) = 3$. In each of these self-similar injectors, the 2nd fractal generation contains m copies that are twice as tall as the 1st generation, with $m = 4$, 6 and 8, respectively, leading to $D = \log(m)/\log(2)$ in each case. The most homogeneous mixing and best overall performance were observed for the intermediate dimension with $m = 6$ and $D = 2.58$, shown in Figure 1a.

However, natural fractal objects are not strictly self-similar mathematical objects, since, at different scales, the mechanisms that determine their formation may not the same. Any natural fractal thus has a finite scaling range. Similarly, fractal objects in engineering need not be strictly mathematically self-similar across all scales, also because some external geometric constraints may make it impossible to satisfy the mathematical scaling rules.[29]

For fractal injectors with a strictly self-similar structure, the fluid jet impingement zone in the central region between vertical outlets from 2nd or higher generation fractal units right above one another, leads to strong anisotropy of the flow field. This is due to an "eclipsed" conformation of vertically neighboring units. To improve the flow field uniformity in a scale-independent manner, the architecture of the fractal injector with $D = \log(6)/\log(2) = 2.58$ can be adjusted without changing its fractal dimension, by simply rotating alternating fractal units by 60^{o}, leading to a "staggered" conformation, which avoids steric hindrance in a similar

manner as for molecular conformations (see Figure 1b). In this paper, the flow field and local turbulence characteristics of the two fractal injectors with eclipsed and staggered fractal architectures are studied through CFD simulations. Results are compared with those obtained for a double-ring sparger, which is set as a control to evaluate the performance of fractal injectors against a traditional mixing device without rotating parts. The macromixing and micromixing performance of the three mixing devices are compared in terms of the turbulence characteristic parameter distribution and concentration field, and the influence of the fractal architecture on the enhancement of mixing process is explored.

2. CFD simulations

2.1 Fractal injector design conformation

Figure 1 illustrates schematically the three fluid injection devices, namely, a staggered fractal injector, an eclipsed fractal injector, and a double-ring sparger. They all comprise 36 nozzles to facilitate the comparison, avoiding any bias due to different fluid injection velocities.

The structure of the eclipsed fractal injector (Figure 1a) has been introduced in our previous work[28], and the difference between staggered and eclipsed fractal injectors can be understood from drawing a parallel with the conformational isomers of ethane. A 2^{nd} generation fractal injector can be characterized by a recursive structure, where two generations of tubes with different sizes can be distinguished. The difference between the 2^{nd} generation eclipsed fractal injector and staggered fractal injector is that, for the two child generation sub-units branching from the same vertical pipes in the parent generation of the staggered fractal injector, tubes in the upper child sub-unit are parallel to those from the parent, while tubes in the lower child sub-unit are rotated by 60^{o} around the vertical axis (Figure 1b), instead of parallel for the eclipsed injector (Figure 1a).

The other geometric parameters are the same for both fractal injectors. In a child generation, the tube diameter, d_2 = 3 mm; the nozzle diameter, $d = d_2$; the length of the horizontal tubes, $e_2 = 2.5d_2$; and the length of the vertical tubes, $l_2 = 7.715d_2$. Compared to the parent generation, the scaling ratio $b = l_2/l_1 = e_2/e_1 = d_2/d_1 = 0.5$. The mounting height h of both fractal injectors is 15.43d (the height from the bottom of the fractal injector to the bottom of the vessel).

For the double-ring sparger, the diameter of the inside ring sparger is T/3, with 12 equidistant, identical nozzles, and the diameter of the outside ring sparger is 2T/3, with 24 equidistant, identical nozzles. The diameter of the nozzles is the same as that of fractal injector (d), and the mounting height of double-ring sparger is also the same, so the location of nozzles is h = 15.43d above the bottom of the vessel.

The diameter of the vessel, T = 22.2 d, and the height of the vessel, H = 69.3 d. The injection velocity, u_j, and injection Reynolds number, Re_j, for these three cases are controlled to be the same, u_j = 1.0 m/s and Re_j = 3000, corresponding to the same total flowrate as well, since the total number of nozzles is 36 in all cases. The vessel always remains filled with liquid: fresh liquid enters the vessel through the fractal injector, and leaves through the top surface, keeping the total amount of liquid in the vessel constant.

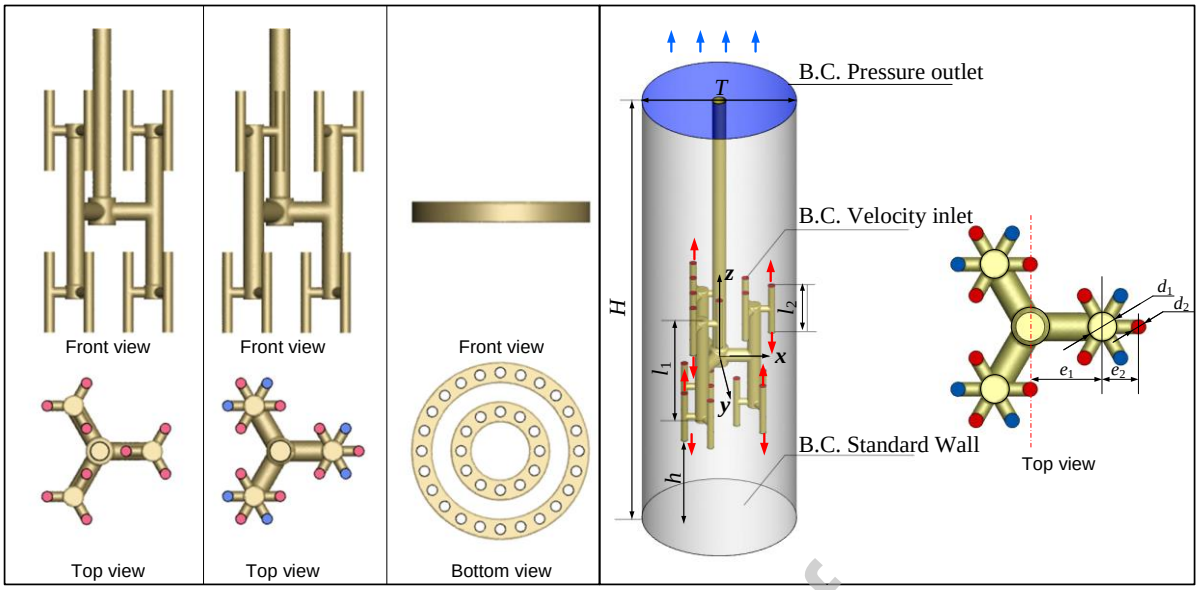

FIGURE 1 Schematic illustrations of (a) eclipsed fractal injector, (b) staggered fractal injector, (c) double-ring sparger, (d) setup of the liquid mixing system, shown for the staggered fractal injector, as used in computational fluid dynamic (CFD) studies (B.C. = boundary condition).

2.2 Governing equations

For complex flows, e.g. the transverse jet or jet in crossflow, the unsteady Reynolds-averaged Navier-Stokes (URANS) simulation is able to capture and reveal the typical vortical structures more accurately than the steady RANS simulation.[30, 31] Therefore, the three-dimensional unsteady Reynolds-averaged Navier-Stokes (URANS) equations were used to analyze the fluid flow and mixing characteristics, and the commercial software package ANSYS Fluent 19.2 was employed in this paper. The governing equations, namely, the continuity equation, momentum equation, and species transport equations were solved for incompressible, turbulent flow conditions.

The continuity equation and momentum equation in the steady state are given by:

$$\nabla \cdot \boldsymbol{u} = 0 \tag{1}$$

$$\rho \boldsymbol{u} \cdot \nabla \boldsymbol{u} = -\nabla p + \nabla \cdot \left[\mu (\nabla \boldsymbol{u} + (\nabla \boldsymbol{u})^T) \right] \tag{2}$$

In the above equations, ρ is the fluid density, t is the physical flow time, $\boldsymbol{u}$ is the velocity vector, p is the pressure, and μ is the fluid viscosity. The renormalization group k–ε (RNG) model is used.[32] This modification of the standard k–ε model improves the description of viscous flows at low Reynolds numbers and for rotational flow.[33] In our previous work[28, 34], the RNG model has been validated by successfully predicting the hydrodynamic flow field of submerged, liquid multi-jets by particle image velocimetry (PIV) experiments; therefore, it is employed in the present work to simulate the flow field. The turbulence kinetic energy, k, and turbulence dissipation rate, ε, satisfy the following equations:[32, 35]

$$\frac{\partial}{\partial t}(\rho k)+\nabla\cdot(\rho k\boldsymbol{u})=\nabla\cdot[(\mu+\frac{\mu_t}{\sigma_k})\nabla k]+\mu_t S^2-\rho\varepsilon \tag{3}$$

$$\frac{\partial}{\partial t}(\rho \varepsilon)+\nabla\cdot(\rho\varepsilon\boldsymbol{u})=\nabla\cdot[(\mu+\frac{\mu_t}{\sigma_\varepsilon})\nabla \varepsilon]-\frac{C_{\varepsilon 1}\varepsilon}{k}P_k-C_{\varepsilon 2}^{*}\rho\frac{\varepsilon^2}{k} \tag{4}$$

where $C_{\varepsilon 2}^{*}$ is the modified coefficient, which can be expressed as follows:

$$C_{\varepsilon 2}^{*}=C_{\varepsilon 2}+\frac{C_\mu\eta^3(1-\eta/\eta_0)}{1+\beta\eta^3} \tag{5}$$

In the above equation, η can be written as $\eta = Sk/\varepsilon$, where S is the modulus of the mean rate-of-strain tensor with elements S_{ij}: $S = (2S_{ij}S_{ij})^{1/2}$, $S_{ij}=\frac{1}{2}(\frac{\partial u_j}{\partial x_i}+\frac{\partial u_i}{\partial x_j})$. The default values of the constants were adopted based on the RNG theory, C_μ = 0.0845, σ_k = 0.7194, σ_ε = 0.7194, $C_{\varepsilon 1}$ = 1.42, $C_{\varepsilon 2}$ = 1.68, η_0 = 4.38, and β = 0.012.

The species transport equation of species i is given by:

$$\frac{\partial(\rho Y_i)}{\partial t}+\nabla\cdot(\rho\boldsymbol{u}Y_i)=-\nabla\cdot\boldsymbol{J_i}+R_i+S_i \tag{6}$$

Here, Y_i and $\boldsymbol{J_i}$ are the local mass fraction and the diffusion flux of species i, respectively. R_i represents the production rate of species i by chemical reaction, and S_i is the species source term. Furthermore, under turbulent flow condition, $\boldsymbol{J_i}$ can be calculated via:

$$\boldsymbol{J_i} = -(\rho D_{i,m} + \frac{\mu_t}{Sc_t})\nabla Y_i \tag{7}$$

where $D_{i,m}$ denotes the mass diffusion coefficient of species i, and Sc_t and μ_t are the turbulent Schmidt number and the turbulent viscosity, respectively.

The Finite Rate/Eddy Dissipation model (FR/EDM) is selected for describing the parallel competitive reactions on a volumetric basis. This model calculates and compares the finite reaction rate and turbulence flow rate to determine the controlling step of the reaction.

The Finite-Rate (FR) model ignores the effect of turbulent fluctuations, instead assuming that the fluid mixing rate is high enough, so that the intrinsic reaction kinetics control the observed, effective reaction rate. The expression of the intrinsic reaction rate of species i in reaction r is given as follows:

$$R_{i,r}^{r} = (v''_{i,r} - v'_{i,r})(k_{f,r}\prod_{j=1}^{N}[C_{j,r}]^{n'_{j,r}} - k_{b,r}\prod_{j=1}^{N}[C_{j,r}]^{n''_{j,r}}) \tag{8}$$

where $k_{f,r}$ and $k_{b,r}$ represent the forward and backward reaction-rate constant, respectively. $v'_{i,r}$ and $v''_{i,r}$ are the stoichiometric coefficient for reactant i and product i, respectively. $C_{j,r}$ denotes the molar concentration of species j. $n'_{j,r}$ and $n''_{j,r}$ are rate exponents for the reactant species j and product species j, respectively. However, considering the fact that the chemical reactions are molecular-level processes, occurring at scales that are much smaller than the grid size, while CFD simulations can only obtain values for $C_{j,r}$ in each grid cell, a micromixing

model is employed to modify Equation (8).

When micromixing affects the overall reaction rate, the FR model needs to be modified. The engulfment-deformation-diffusion (EDD) model was proposed by Baldyga et al.[36, 37] to describe the micromixing process, which was based on the mechanisms of engulfment (at the Kolmogorov scale), deformation and diffusion (from the Kolmogorov scale up to the Batchelor scale). When the Schmidt number in the system is less than 4000, the EDD model

can be simplified to the engulfment model (E-model), which takes the engulfment process as the controlling step of micromixing and neglects the deformation and diffusion processes[36]. The core premise of the E-model is that mixing between two fluid elements by engulfment is formulated by the feeding eddies and the step will periodically occur over a certain number of generations until perfect micromixing is finally obtained. The equations of the E-model are shown as follows:

$$\frac{dV}{dt} = EV \tag{9}$$

$$\frac{dC_i}{dt} = E(C_{iE} - C_i) + R_{i,r}^r \tag{10}$$

where E is the engulfment rate, which can be determined by [38]:

$$E = 0.058(\varepsilon / \nu)^{0.5} \tag{11}$$

In the above equations, V represents the volume which is micromixed; C_i and $C_{i\mathrm{E}}$ denote the molecular concentration of species i in the reaction region and the averaged molecular concentration of species i in the ambient fluid, respectively; ν is the kinematic viscosity.

The Eddy-Dissipation model (EDM) [39] ignores the chemical reaction kinetics, and assumes that the overall source of chemical species i is controlled by the turbulent mixing, which can be expressed by:

$$R_{i,r}^t = \nu_{i,r}^{'} M_i A \rho \frac{\varepsilon}{k} \min\left[\min_R \left(\frac{Y_R}{\nu'_{R,r} M_R} \right), \frac{B \sum_P Y_P}{\sum_j^N \nu''_{j,r} M_j} \right] \tag{12}$$

where the subscripts R and P stands for reactant and product, respectively; M_i and M_j denote the molecular weight of reactant i and product j; A and B are empirical constants used to evaluate the factors of diffusion and spreading of flames (EDM is designed for combustion reactions). For the liquid reaction system in this work, the spreading of flames should be neglected (set B = 0), and the turbulent mixing rate $R_{i,r}^t$ needs to be adjusted. The default

value of constant *A* is 4.0, which has been used in a number of CFD simulation works, albeit without validation.[39] Indeed, the value of *A* is not trivial. Wang et al.[40] carried out a series of numerical investigations of this model constant. Compared with the experimental data, they noted a large simulation error for $A = 4.0$, especially for round jet flames with weak turbulence, while, for $A = 1.0$, the simulations accurately predicted the axial temperature distribution of the round jet ($Re = 10000$). By just modifying the value of the constant *A*, Ouyang et al.[41] found that *A* is determined by the operating parameters, and the error between the simulation and experimental results was less than 20 % when $Re = 4155$ ($A = 1.0$), and less than 10% for $Re = 334 \sim 668$ ($A = 0.7$). Considering that the jet injection Reynolds number $Re_j = 3000$ in the present system, it is within the range of tested Reynolds numbers, and the mixing rate is adjusted by setting the value of constant *A* to 1.0. The main conclusions of this paper remain the same for $A = 0.7$, however, it should be noted that a different value for *A* leads to different numerical results, something that should be checked experimentally in the future.

Therefore, the modified FR/EDM can be described by:

$$R_i = \sum R_{i,r} = \sum \min(R_{i,r}^{r-E}, R_{i,r}^{t}) = \sum \min(E(C_{iE} - C_i) + R_{i,r}^{r}, \nu_{i,r}^{'} M_i \rho \frac{\varepsilon}{k} \min_R(\frac{Y_R}{\nu'_{R,r} M_R})) \quad (13)$$

where R_i is the net source of *i*, $R_{i,r}$ is the net source of *i* in reaction *r*, and $R_{i,r}^{r-E}$ is the reaction rate of species *i* in reaction *r*, accounting for micromixing, as in Equation (10).

2.3 Simulation conditions

In this work, steady-state RANS flow simulations were first performed to obtain the initial flow field. Both the injected fluid and the initial fluid in the vessel were set as pure water at 298 K (density $\rho = 998.2$ kg/m^3, dynamic viscosity $\mu = 10^{-3}$ Pa·s). Gravity was accounted for in all simulations, and the *z* axis is directed against gravity. Then, the simulations solver was

switched to transient-state, and the computational time step was 0.0004 s, which ensured that the Courant number was less than 0.8. The averaged URANS results were obtained after the simulated physical time reached 30 s. Results that employed averages using 30 frames, 40 frames and 50 frames, with a time interval of 0.1 s between adjacent frames, were compared. Only minor differences were observed between the results obtained with 40 and 50 frames, which indicated that the number of frames did not affect the results when it was at least 40. For this reason, the average URANS results with 40 frames were used. Next, transient simulations of the transport equations were carried out to investigate the mixing process, where local micromixing was considered by introducing the modified FR/EDM (coupled with the E-model). At time t = 0 s, the reactant/tracer was injected into the vessel. Here, the simulation time step was fixed at 0.0004 s. The calculations of species transport were stopped when t = 1.0 s. The physical properties of the solution were assumed to be identical to water at 298 K, with a molecular diffusivity $D_m = 10^{-9}$ m^2/s for each species.[42] The effect of the reaction heat was neglected, and the temperature in the calculation domain was assumed to be constant (298 K).

All the inlets were set as velocity inlet boundary condition, and an ideal uniform inlet velocity distribution was assumed. The pressure outlet boundary condition was selected for the outlet at the top surface of the vessel. Both the walls of the vessel and the injectors were specified as standard no-slip wall boundary condition.

The SIMPLEC algorithm was applied to solve the pressure-velocity coupling flow field. A Green-Gauss cell and PRESTO! scheme were implemented for gradient and pressure discretization. A second-order upwind scheme was applied to solve the spatial discretization of the momentum, turbulent characteristics, and all species transport equations. For all equations, the residuals were at most 10^{-6}.

2.4 Mesh independence test

The injector structures and simulation grids were created in Gambit 2.4.6 (ANSYS Inc.). As illustrated in Figure 2, the mesh was composed of unstructured tetrahedral cells. The local grid was refined around the nozzles, and the grid for the boundary layer at the region near the wall of the vessel was encrypted to 10 layers.

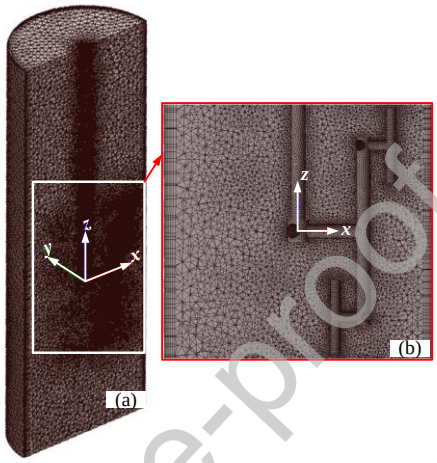

FIGURE 2 (a) Scheme of computational grid; (b) close-up of the local region around the nozzles.

To ascertain that the simulation results were grid-independent, the effect of three mesh schemes with different average mesh sizes 2.5 mm (23 million cells), 3.0 mm (20 million cells), and 4.0 mm (19 million cells) were evaluated. Figure A1 (Supporting Information-Part A) shows the velocity and concentration profiles for the staggered fractal injector with the three different mesh schemes. No significant differences in the values of the velocity and concentration occurred when the average mesh size decreased from 3.0 mm to 2.5 mm. Therefore, to lessen the calculation burden, the global mesh size was set to 3.0 mm in this work, and the corresponding total cell number is about 20 million.

3. Mixing performance characteristics

According to the scale levels at which mixing occurs, mixing can be divided into three parallel mechanisms: macromixing, mesomixing, and micromixing. Macromixing occurs at the reactor scale, which can be expressed by the residence time distribution. It controls species transport in the whole reactor. Mesomixing occurs on scales that are smaller than bulk circulation, but larger than the micromixing scale. The mesomixing time of chemical reactions generally depends on the turbulence behavior at the feeding inlet and the inlet velocity. Micromixing occurs close to the molecular scale, and it affects the selectivity of the products. The micromixing and reaction kinetics co-determine the yield of the desired products.[33]

3.1 Macromixing index

To quantify and analyze the macromixing behavior, the standard deviation of the tracer mass fraction in the vessel was calculated. The standard deviation of the tracer mass fraction is affected by the intensity of segregation, using the volume-averaged tracer mass fraction w_{av} at time t, where w_{av} is defined as follows:

$$w_{av} = \frac{\sum_{m=1}^{N_c} V_m w_m}{\sum_{m=1}^{N_c} V_m} = \frac{\sum_{m=1}^{N_c} V_m w_m}{V_{total}} \tag{14}$$

In the above equation, N_{c} represents the number of cells in the calculation domain, V_m is the volume of cell m, V_{total} is the total effective volume of the vessel (without the volume occupied by the injector), and w_m denotes the tracer mass fraction in cell m at time t. The standard deviation of the tracer mass fraction σ_w at time t is defined as:

$$\sigma_w = \sqrt{\frac{\sum_{m=1}^{N_c} V_m (w_m - w_{av})^2}{V_{total}}} \tag{15}$$

A small value of σ_w indicates better mixing uniformity, and the value of this standard deviation is zero for perfect mixing.

4.2 Micromixing index

A parallel competing reaction system, the Villermaux/Dushman system, is employed in this paper to quantitatively assess the micromixing efficiency. It was first proposed by Fournier et al.[43, 44], and is one of the most widely used test reaction systems for many mixing devices. The Villermaux/Dushman system consists of the following reactions:

$$H_2BO_3^- + H^+ \rightarrow H_3BO_3 \text{ (quasi-instantaneous)} \quad \text{(i)}$$

$$5I^- + IO_3^- + 6H^+ \rightarrow 3I_2 + 3H_2O \text{ (fast)} \quad \text{(ii)}$$

$$I^- + I_2 \leftrightarrow I_3^- \quad \text{(iii)}$$

The kinetic model developed by Guichardon et al.[45] is adopted, where reaction (i) is a quasi-instantaneous neutralization reaction, and its kinetics can be expressed as:

$r_1 = k_1[H^+][H_2BO_3^-]$, with kinetic constant $k_1 = 10^{11}$ m^3/(kmol·s).

Reaction (ii) is a fast redox reaction, which is slower than reaction (i), and its kinetics are written as:

$r_2 = k_2[H^+]^2[IO_3^-][I^-]^2$; the kinetic constant k_2 of reaction (ii) depends on the ionic strength I of the medium in the vessel[46]:

$$\log k_2 = \begin{cases} 9.28 - 3.66\sqrt{I} & I < 0.16 \text{ kmol/m}^3 \\ 8.38 - 1.51\sqrt{I} + 0.23I & I > 0.16 \text{ kmol/m}^3 \end{cases} \quad (16)$$

Reaction (iii) is an instantaneous equilibrium reaction and can be described as:

$r_3 = k_{3+}[I^-][I_2] - k_{3-}[I_3^-]$, where $k_{3+} = 5.9 \times 10^9$ m^3/(kmol·s), and $k_{3-} = 7.5 \times 10^6$ 1/s.

In order to quantify the micromixing efficiency, the segregation index (X_s) is defined as follows:

$$X_S = \frac{Y}{Y_{ST}} \tag{17}$$

$$Y = 2(n_{I_2} + n_{I_3^-}) / n_{H^+} \tag{18}$$

$$Y_{ST} = \frac{6[IO_3^-]_0}{6[IO_3^-]_0 + [H_2BO_3^-]_0} \tag{19}$$

Here, Y denotes the ratio of the H^+ consumed by reaction (ii) to the total H^+ injected into the system. n_{I_2} and $n_{I_3^-}$ are the molar quantities of the I_2 and I_3^- in the vessel at time t, respectively. Y_{ST} is the value of Y in case of complete segregation. The value of X_S changes between 0 and 1 for partial segregation; the lower the value of X_S, the better the micromixing performance. The subscript 0 stands for the initial concentration of species. In this work, the initial concentration of the reactants is listed in Table B1 of Supporting Information-Part B.[46]

The overall conversion of reactant $H_2BO_3^-$, $X_{H_2BO_3^-}$, is adopted as a quantitative index for describing the micromixing effect:

$$X_{H_2BO_3^-} = \frac{n_{H_2BO_3^-,0} - n_{H_2BO_3^-}}{n_{H_2BO_3^-,0}} \tag{20}$$

where $n_{H_2BO_3^-,0}$ and $n_{H_2BO_3^-}$ are the molar quantities of $H_2BO_3^-$ in the vessel at time 0 and t, respectively.

Since the injected acid only reacts with the reactants in the fluid surrounding the nozzles, X_S can be used to indicate the local micromixing near the nozzles, but it cannot be used directly to calculate the micromixing time. The characteristic micromixing time, t_m, refers to the time needed to achieve uniform mixing on the molecular scale, and the hydrodynamic conditions determine the micromixing time. In the E-model, the micromixing time t_m can be calculated by:[47]

$$t_m = \frac{1}{E} = 17.24\left(\frac{\nu}{\varepsilon}\right)^{0.5} \tag{21}$$

4. Results and discussion

4.1 Flow field analysis

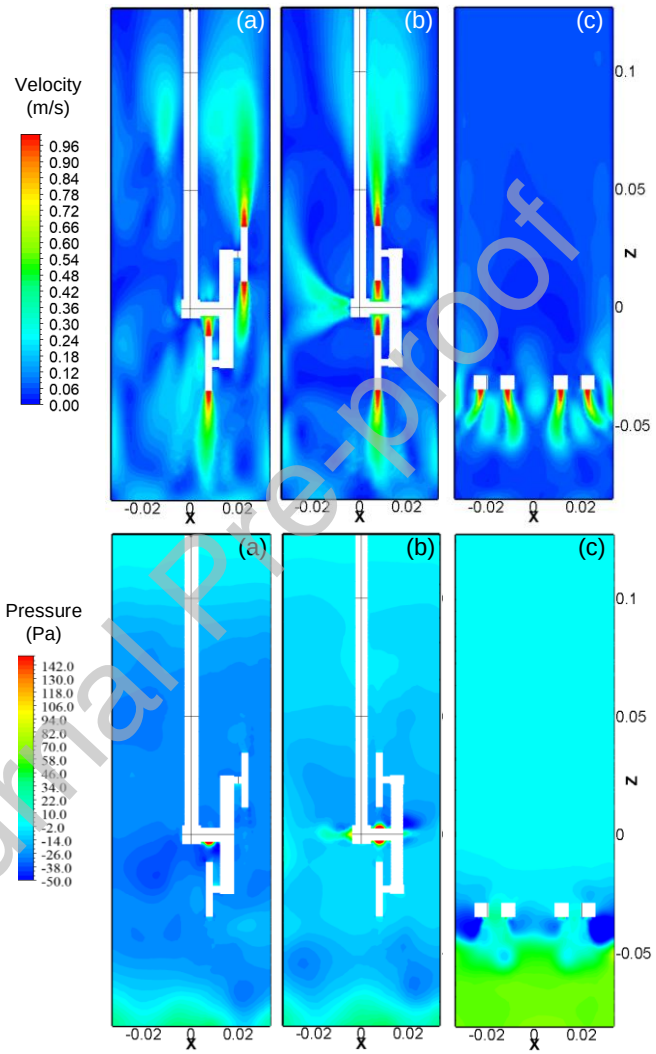

FIGURE 3 Contours of the velocity and pressure distribution in slice $y = 0$ with (a) staggered fractal injector, (b) eclipsed fractal injector, and (c) double-ring sparger.

Figure 3 displays the contours of the velocity magnitude and pressure for the three mixers at $Re_j = 3000$. It can be observed in Figure 3a that, for the staggered fractal injector, the cross

jet flow and co-current jet flow coexist in the flow field; in the central region, part of the jets impact the wall of the horizontal pipes, which leads to the appearance of a high pressure region. There are no obvious radial jets in the case of a staggered fractal injector. For the eclipsed fractal injector, as shown in Figure 3b, there are parallel multiple jets and a jet impingement zone. In the central region, the jets are deflected by the impingement, and the direction of the jets changes from vertical to radial around the impinging surface, where a high-pressure zone can be observed. For the double-ring sparger (Figure 3c), since all the nozzles are mounted in the same horizontal plane and are close to the bottom wall, the adjacent parallel jets interact with each other, the central line of the jets deflect and the jets tend to merge. The flow field shows significant asymmetry in the vertical direction.

Figure 4 presents streamlines for the three mixers. The direction of flow is indicated by the red arrows on the streamlines. For both fractal injectors, strong circulation can be found in the upper and lower parts of the vessel, while Figure 4c indicates that there is no circulation loop in the vessel where a double-ring sparger is used. In addition, when comparing Figure 4a and Figure 4b, more large-scale circulation loops can be observed in the case of a staggered fractal injector, while there are small circulation loops around the impingement zone of the eclipsed fractal injector.

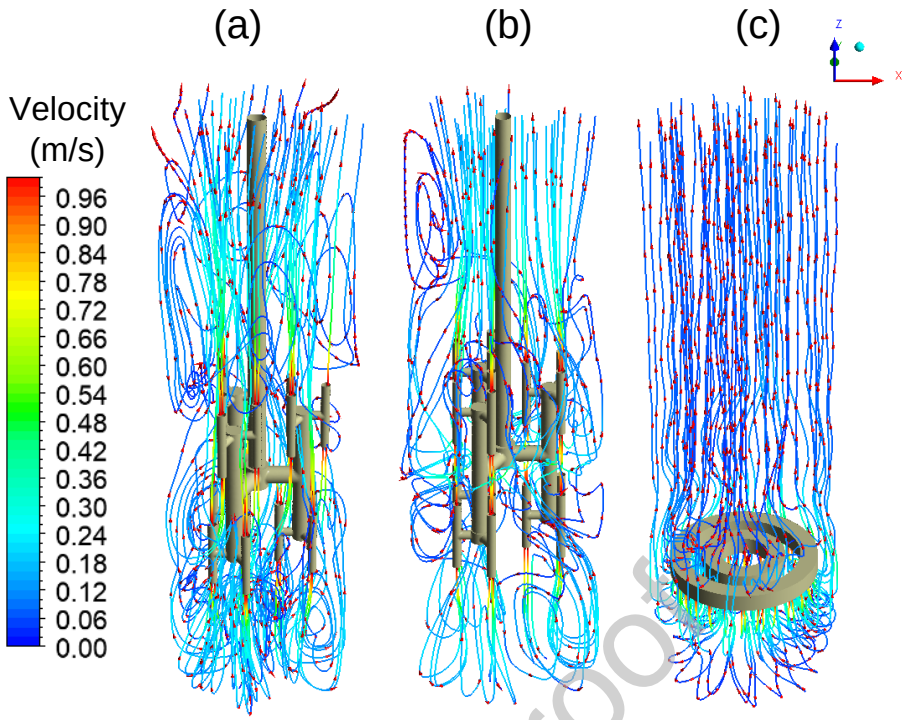

FIGURE 4 Streamlines of (a) staggered fractal injector, (b) eclipsed fractal injector, and (c) double-ring sparger.

The turbulence kinetic energy (TKE), *k*, is a key indicator for mass transfer enhancement and plays an important role in controlling the observed chemical reaction rates and selectivity[48]. The distribution of *k* for the three mixers is illustrated in Figure 5. For the staggered fractal injector, the generated TKE dissipates in the shear layers of the jets in which the surrounding fluid is entrained, and the high TKE region is located near the horizontal pipes which are impacted by the jets. For the eclipsed fractal injector, in slice $z = 0$, the distribution of TKE is quite uniform; the impingement jets meet in the central region, where the produced turbulence energy dissipates promptly by impingement between fluid streams. However, in the upper and lower parts of the vessel, *k* is distributed unevenly, which can be explained by the smaller circulation loops (Figure 4). Therefore, on the whole, the *k* distribution of the staggered fractal injector is more uniform. For the double-ring sparger, the strong TKE is mainly concentrated near the horizontal plane where the nozzles are located.

The asymmetric distribution of *k* reveals laminar and turbulent flow regimes in the upper and lower parts of the vessel, respectively.

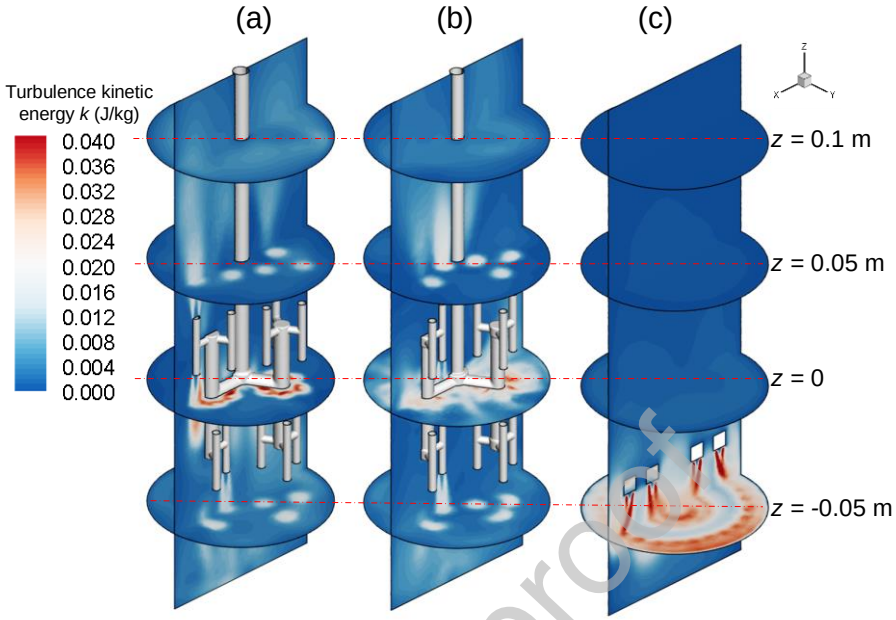

FIGURE 5 The contours of the *k* distribution in slice *y* = 0 and slices *z* = -0.05, 0.00, 0.05, and 0.10 m with (a) staggered fractal injector, (b) eclipsed fractal injector, and (c) double-ring sparger.

The turbulent structures can also be quantified by the Q-criterion, defined as follows:[49]

$$Q = \frac{1}{2}(\| \boldsymbol{\Omega} \|^2 - \| \boldsymbol{S} \|^2) \tag{22}$$

In the above equation, $\boldsymbol{\Omega}$ and $\boldsymbol{S}$ denote the vorticity and the strain rate tensor, respectively. *Q* represents the local balance between shear strain rate and vorticity magnitude, defining vortices as areas where the magnitude of the vorticity is greater than the magnitude of the strain rate, and the positive values of *Q* are indicative of areas in the flow field where the vorticity dominates.

Figure 6, which compares the three mixing devices for the same value of *Q*, points out significantly different behaviors. For the staggered fractal injector, a spiral vortex structure can be found in the region near the nozzles at the top and bottom of the injector, while, in the

central region, due to the opposing jets, the spiral vortex structure deforms quickly in the downstream of the jet injection, and a vortex tube-like structure can be observed, which indicates that there are effective interactions between adjacent jets. The main difference between the vortex structures induced by the two fractal injectors is the structure in the center: in the eclipsed fractal injector, the double toroidal vortices are characterized by a pair of vortex rings rotating in opposite directions, due to the collision between the upward and downward jets.[28] Finally, for the double-ring sparger, the results reveal a large vortex ring rotating counterclockwise, which dominates the turbulent structure.

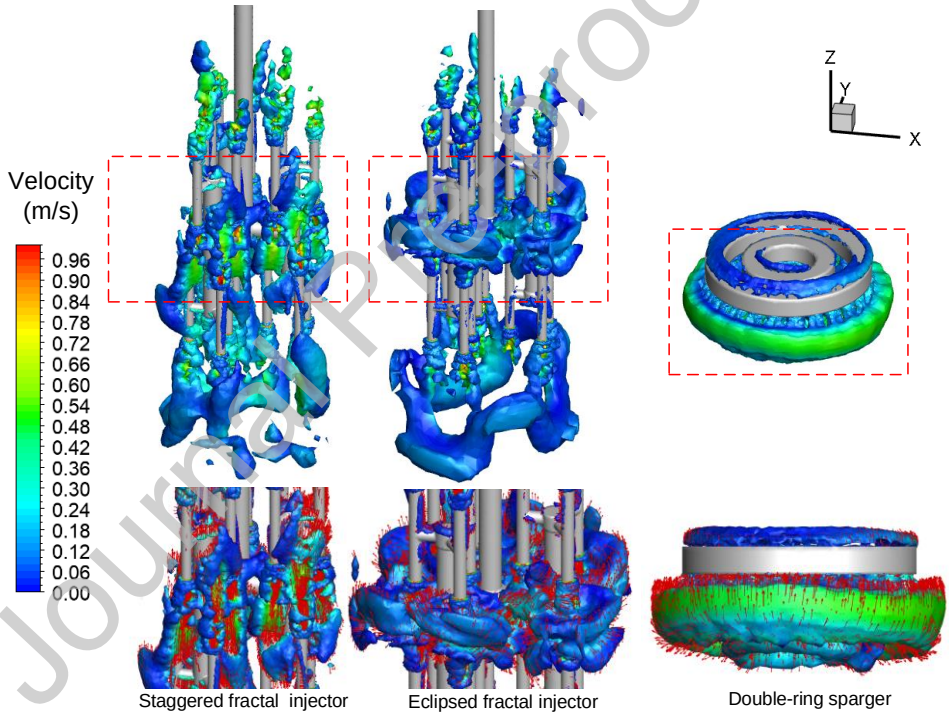

FIGURE 6 Iso-surfaces of Q = 0.05, colored by velocity. Magnified images of the iso-surfaces in the bottom row are overlaid with velocity vectors.

4.2 Macromixing performance analysis

The macromixing process was visualized by adding a tracer. The physical properties of this tracer were assumed to be the same as those of water, and the diffusion coefficient was set as

10^{-9} m^2/s.[50] At t = 0.0 s, the injected fluid was changed from water to tracer with a mass fraction of 100%.

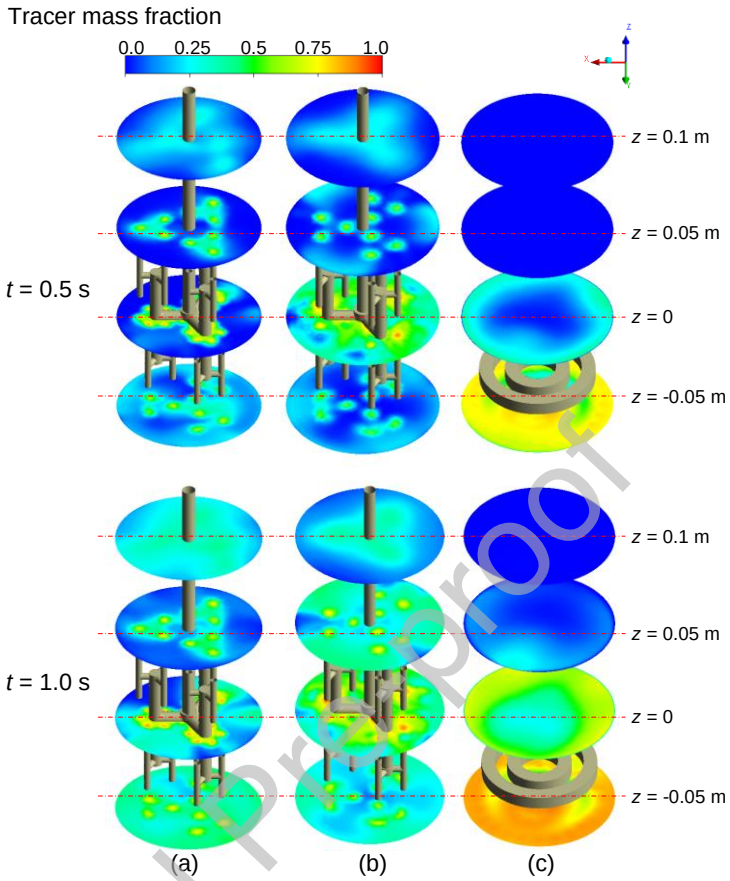

FIGURE 7 Tracer mass fraction profiles in four slices, z = -0.05, 0.00, 0.05, and 0.10 m, for (a) staggered fractal injector, (b) eclipsed fractal injector, and (c) double-ring sparger.

The spreading of the tracer in the vessel is due to advection and diffusion; both of these processes are important for jet mixing, which is evident in the tracer concentration contours shown in Figure 7. Of the two conformations of fractal injector, the eclipsed one shows better mixing performance in the central region, because there is an impingement zone; therefore, the local turbulence is stronger, and the mixing in radial direction is better. However, for the region downstream of the jets (slices z = -0.05 and 0.10 m), the staggered fractal injector shows better mixing performance. This can be explained by the larger value of the average velocity in the vessel containing a staggered fractal injector, where the entrainment between

the jets and the surrounding fluid is enhanced by the interaction between the parallel jets (Figure 6), and the turbulence in these regions is stronger (Figure 5). Finally, for the double-ring sparger, there is no large circulation loop in the vessel, and the upper part of the vessel is a low-velocity region (dead zone), making it difficult to achieve macromixing by convection. Spreading in the upper part occurs mostly by diffusion, leading to poor macromixing there, and the tracer accumulates in the region near the bottom.

To quantitatively compare the macromixing performance, probability density distributions of the tracer mass fraction, w, were obtained, as shown in Figure 8. The probability density distribution of an ideal mixer is a Dirac pulse, $\delta(w)$, and is also shown in Figure 8: the composition throughout an ideally mixed vessel is instantaneously uniform, so that, at any time t, the probability is 1 for w = (total inlet mass flowrate * t) / (total mass of liquid in the vessel). On the whole, the macromixing performance of the staggered fractal injector is similar to that of the eclipsed fractal injector. However, over time, the distribution for the staggered fractal injector has a narrower peak, and its peak location is close to the ideal mixer (Figure 8b). This difference can be explained by the more uniform flow field in the staggered fractal injector system, and the contours of the tracer mass fraction also indicate that the tracer more easily accumulates in the central region for the eclipsed fractal injector (Figure 7b). The probability density distribution for a double-ring sparger is significantly different from that of the fractal injectors: there are two peaks located at high values of w, and the difference becomes more significant over time. For the double-ring sparger, the flow field can be divided into laminar and turbulent flow regions, and mixing in the upper laminar flow region can only be achieved by diffusive mixing, therefore the tracer tends to accumulate in the region near the bottom wall, as shown in Figure 7c.

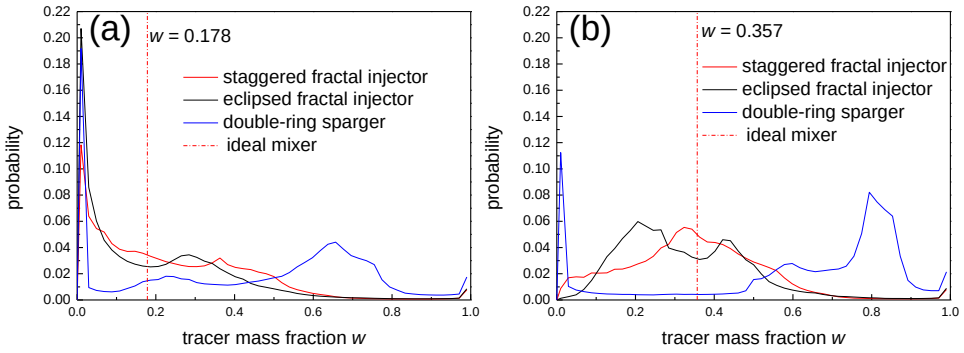

FIGURE 8 Comparison between the probability density distributions of the tracer mass fraction, w, at (a) t = 0.5 s and (b) t = 1.0 s.

The standard deviation of the tracer mass fraction was normalized by w_{av} to compare the results across mixers with a different architecture. It can be observed from Figure 9 that at the initial stage, the staggered fractal injector can achieve the smallest value of $\boldsymbol{\sigma_w/w_{av}}$, the curves of the staggered and eclipsed fractal injector almost overlap when t > 0.6 s, and the normalized standard deviation of the tracer mass fraction when using a fractal injector is smaller than for the double-ring sparger during the mixing process. This indicates that the staggered conformation improves the mixing uniformity in the initial stage of mixing, however, its effect will decrease over time, and the mixing uniformity of a fractal injector is obviously better than that of a double-ring sparger.

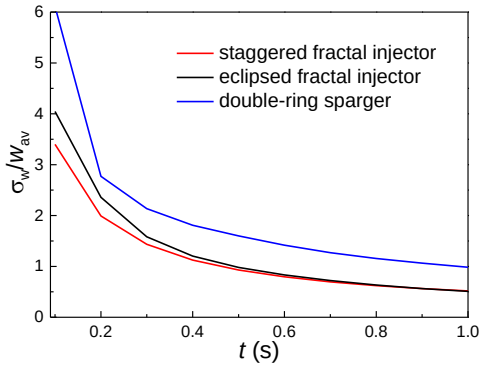

FIGURE 9 Normalized standard deviation of the tracer mass fraction σ_w/w_{av} as a function of mixing time t.

4.3 Micromixing performance analysis

Figure 10 shows the contours of the molecular concentration of the main product, H_3BO_3, at t = 0.4s. These were simulated using the modified FR/EDM, involving the E-model for the three mixers. Because reaction (i) is quasi-instantaneous, the injected sulfuric acid will be rapidly consumed to form H_3BO_3. In the region near the nozzles, the concentration of H_3BO_3 is very low. The product H_3BO_3 is mainly distributed in the shear layer and merging region of the jets, where the mixing and interactions between jets and ambient flow take place.[51] It can be seen that the staggered fractal injector has the most uniform distribution of H_3BO_3. For the eclipsed fractal injector, the concentration of H_3BO_3 in the central region is higher, which is due to the stronger turbulence and higher mixing quality in this impingement zone. Finally, for the double-ring sparger, H_3BO_3 is mainly concentrated in the turbulent, lower region of the vessel.

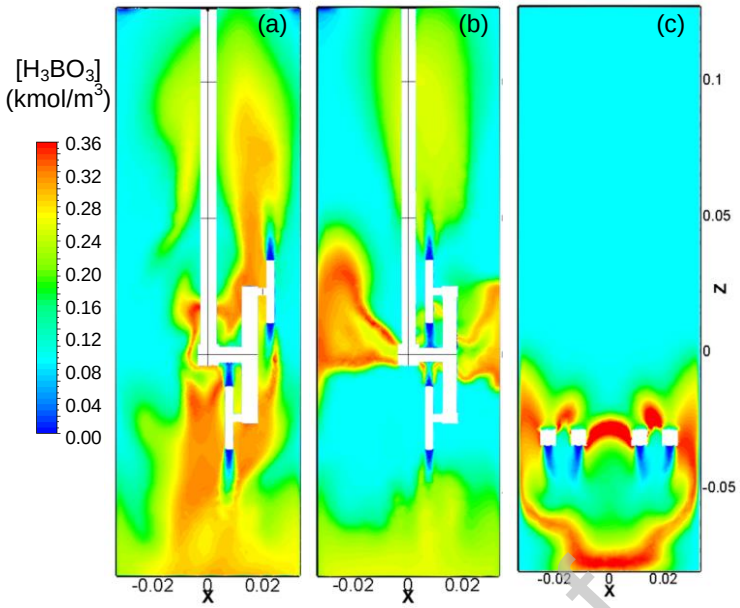

FIGURE 10 Contours of the concentration of H_3BO_3, within vertical slice $y = 0$, at $t = 0.4$ s, for (a) staggered fractal injector, (b) eclipsed fractal injector, and (c) double-ring sparger.

Another way to quantify the micromixing is shown in Figure 11, which presents the segregation index, X_s, as a function of flow time t for the three mixers. For the double-ring sparger system, the X_s curve shows a different trend and larger values than the curves for both fractal injectors. The staggered fractal injector leads to a smaller X_s than the eclipsed fractal injector, which demonstrates that micromixing is enhanced by adjusting the conformation of the fractal injector to be staggered and further indicates that the overall interactions between the jets and the ambient fluid are more effective for the staggered fractal injector.

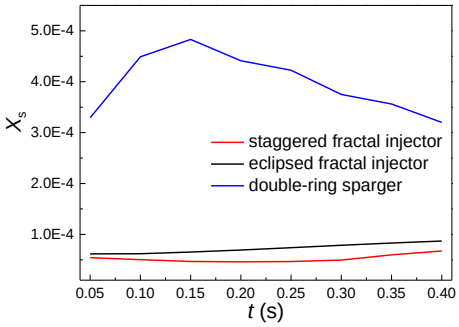

FIGURE 11 Micromixing segregation index, X_s, as a function of time, for the two fractal injectors and the double-ring sparger.

The evolution over time of the conversion of the main reactant ($H_2BO_3^-$), X_{H2BO3-}, for the three mixers is shown in Figure 12. The slopes of the curves for the staggered and eclipsed fractal injectors soon become similar, however, the value of the conversion when using a staggered fractal injector is slightly larger than that for an eclipsed fractal injector. In the initial stages, the conversion of the double-ring sparger is similar to that of the fractal injector, but, over time, the difference between the double-ring sparger and the fractal injectors becomes significant, and X_{H2BO3-} obtained when using a double ring sparger is obviously smaller than that for a fractal injector. The fast and slow reactions are affected by mixing to different degrees; the larger the contact area between the jet flow and bulk flow (Figure 6), the higher the selectivity to the formation of the main reaction product from the fast reaction.[42] The results reveal that the staggered fractal injector shows the strongest interaction between the jets and the surrounding fluid among the three mixing devices.

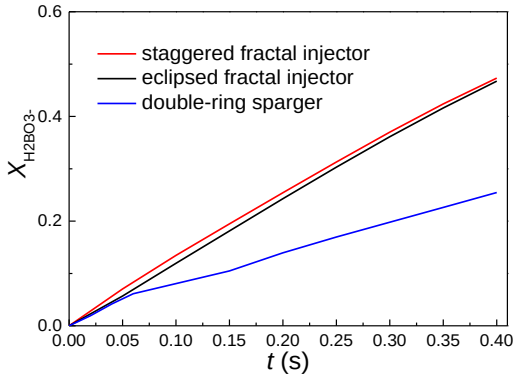

FIGURE 12 Conversion of $H_2BO_3^-$ as a function of time, for the two fractal injectors and the double-ring sparger.

Figure 13 displays the distribution of the micromixing time, t_m, calculated locally by the E-model. Figures 13a and b indicate that the micromixing time distributions of staggered and eclipsed fractal injectors are quite close, and the micromixing time is distributed uniformly in the whole vessel. Compared with the velocity and kinetic energy distributions (Figure 3a and Figure 5), the regions with shorter local micromixing time are characterized by higher fluid velocities and turbulence intensity, which can also be observed in the complicated vortex structures. For the double-ring sparger, the value of t_m in the region above the device is much larger than that in the turbulent region below the device.

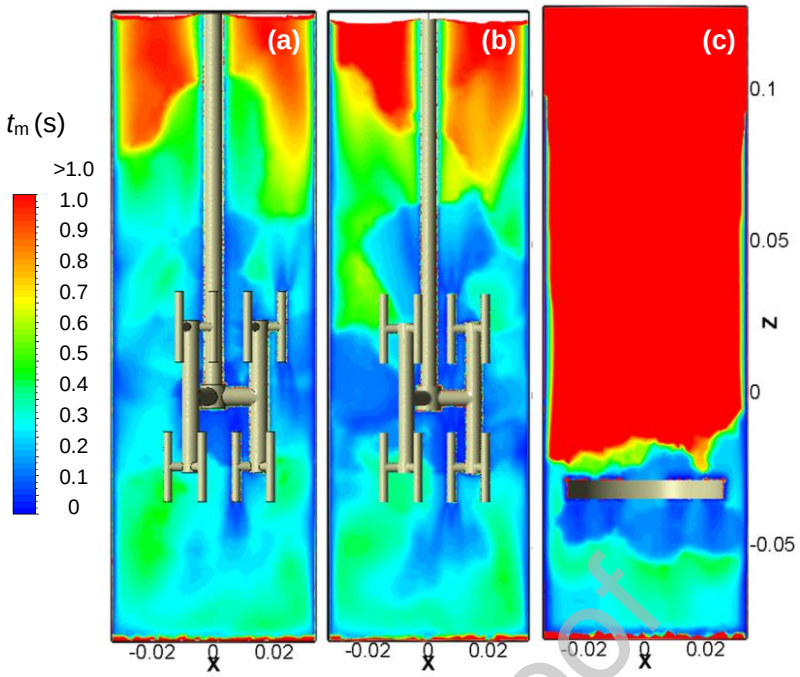

FIGURE 13 Contours of the micromixing time, t_m, presented within vertical slice $y = 0$, at $t = 0.4$ s, for (a) staggered fractal injector, (b) eclipsed fractal injector, and (c) double-ring sparger.

In the Villermaux/Dushman system, H^+ is the reactant of reaction (i) and (ii), and the reaction region can be determined according to the concentration distribution of H^+ in the vessel. The reaction region is affected by the mixing and reaction processes, and its volume will expand due to advection, engulfment, deformation, and diffusion. The region's volume will decrease due to the consumption of reactants.[38] In this work, the reaction region is marked by a critical concentration of H^+, where $[H^+] > 10^{-10}$ kmol/m^3. At $t = 0.4$ s, the normalized volume of the reaction region (normalized by V_{total}, the total effective volume of the vessel) for a staggered fractal injector, eclipsed fractal injector and double-ring sparger is 0.290, 0.338, and 0.217, respectively, and the average micromixing time, $\langle t_m \rangle$, in the reaction region for the staggered fractal injector, eclipsed fractal injector and double-ring sparger is 0.083 s, 0.096 s, and 0.238 s, respectively. The volume of the reaction region for the fractal injectors is larger than that for the double-ring sparger, which illustrates that the

local turbulent flow region around the spatially distributed nozzles is conducive to the expansion of the reaction region. It can also be seen that the average micromixing time decreases, after adjusting the fractal injector to a staggered conformation, which is consistent with the results for the segregation index.

5. Conclusions

In this work, two conformations of a self-similar, fractal injector of dimension D = 2.58 are studied by CFD simulations. This fractal injector is developed for mixing intensification by organizing the local flow structure in reactors where fast liquid mixing is essential, but a rotating mixer is undesired. The intermediate fractal dimension of D = 2.58 was chosen, due to its superior mixing properties over D = 2 and D = 3 in a previous study.[28] A double-ring sparger has been set as the reference to investigate the application of a fractal injector in a process where fast and uniform mixing are required.

The RNG k-ε turbulence model was employed. The simulated flow field illustrates that for the staggered fractal injector, there are co-current and cross jets, although, in the central region, turbulence is weaker than for the eclipsed fractal injector, due to the disappearance of an impingement zone. Also, the distribution of turbulence kinetic energy is more uniform, the local turbulence around the nozzles located near the top and bottom of the vessel is enhanced, and the entrainment of ambient fluid is strengthened.

The liquid mixing process is characterized by macromixing and micromixing, related to different mixing scale levels. The staggered fractal injector shows similar macromixing performance as the eclipsed fractal injector, which reveals that the conformation has little effect on the macromixing performance of the fractal injector. The modified FR/EDM, involving local micromixing by coupling with the E-model, was adopted to investigate the micromixing process. The staggered fractal injector leads to the lowest segregation index and

micromixing time among the three mixing devices, which indicates that the staggered conformation of the fractal injector yields more efficient micromixing than the injector with a strictly self-similar, eclipsed fractal structure.

The comparison between the fractal injectors (spatial distribution of nozzles) and the double-ring sparger (planar distribution of nozzles) confirms the advantages of a fractal injector over a conventional one. Again, it can be found that a fractal injector generates good performance for liquid-liquid systems, with better macromixing uniformity, micromixing performance in the whole vessel, and higher reaction selectivity, stronger interactions between jets and surrounding fluid, and more efficient use of the reactor volume. All of these indicate that the fractal injector is promising to implement liquid mixing process intensification for the chemical industry.

Author contributions

Shuxian Jiang: Data curation; formal analysis; investigation; software; validation; visualization; writing – original draft. **Marc-Olivier Coppens**: Conceptualization; funding acquisition; methodology; project administration; supervision; writing – review & editing. **Jiajun Wang**: Funding acquisition; methodology; resources; supervision; writing – review & editing.

Declaration of interests

The authors declare that they have no known competing financial interests or personal relationships that could have appeared to influence the work reported in this paper.

Acknowledgements

This work was financially supported by the National Key R&D Program of China (2017YFB0307702), the National Nature Science Foundation of China (22078284) and the State Key Laboratory of Chemical Engineering (SKL-ChE-16D02). M.-O. C. is grateful to EPSRC for a “Frontier Engineering” (EP/K038656/1) and “Frontier Engineering: Pro-

egression" (EP/S03305X/1) Awards at UCL, as well as to Zhejiang University for a Qiushi Chair Professorship. S.J. and M.-O. C. thank Synfuels China for funding S.J.'s PhD research.

References

[1] L. Metzger, M. Kind, On the mixing in confined impinging jet mixers–time scale analysis and scale-up using CFD coarse-graining methods, Chem. Eng. Res. Des. 109 (2016) 464-476.

[2] A. Nagaki, K. Kawamura, S. Suga, T. Ando, M. Sawamoto, J.-i. Yoshida, Cation pool-initiated controlled/living polymerization using microsystems, J. Am. Chem. Soc. 126 (2004) 14702-14703.

[3] V.V. Ranade, Towards better mixing protocols by designing spatially periodic flows: The case of a jet mixer, Chem. Eng. Sci. 51 (1996) 2637-2642.

[4] Y. Yu, J. Wu, H. Meng, Numerical simulation process aspects of the novel static circulating jet mixer, Can. J. Chem. Eng. 89 (2011) 460-468.

[5] M.K. Parsa, F. Hormozi, D. Jafari, Mixing enhancement in a passive micromixer with convergent–divergent sinusoidal microchannels and different ratio of amplitude to wave length, Comput. Fluids 105 (2014) 82-90.

[6] V. Kumar, M. Paraschivoiu, K.D.P. Nigam, Single-phase fluid flow and mixing in microchannels, Chem. Eng. Sci. 66 (2011) 1329-1373.

[7] E. López-Guajardo, E. Ortiz-Nadal, A. Montesinos-Castellanos, K.D.P. Nigam, Coiled flow inverter as a novel alternative for the intensification of a liquid-liquid reaction, Chem. Eng. Sci. 169 (2017) 179-185.

[8] S. Soni, L. Sharma, P. Meena, S. Roy, K.D.P. Nigam, Compact coiled flow inverter for process intensification, Chem. Eng. Sci. 193 (2019) 312-324.

[9] A. Soleymani, E. Kolehmainen, I. Turunen, Numerical and experimental investigations of liquid mixing in t-type micromixers, Chem. Eng. J. 135 (2008) S219-S228.

[10] B. Wu, C. Li, M. Zhang, P. Luo, Liquid mixing intensification by adding swirling flow in the transverse jet mixer, AIChE J. 67 (2021) e17276.

[11] H. Zhang, T. Kopfmüller, R. Achermann, J. Zhang, A. Teixeira, Y. Shen, K.F. Jensen, Accessing multidimensional mixing via 3d printing and showerhead micromixer design, AIChE J. 66 (2020) e16873.

[12] J.Z. Luo, G.W. Chu, Y. Luo, M. Arowo, B.C. Sun, J.F. Chen, Regulating the micromixing efficiency of a novel helical tube reactor by premixing behavior optimization, AIChE J. 63 (2017) 2876-2887.

[13] B.B. Mandelbrot, The fractal geometry of nature, W. H. Freeman and Company, New York, 1982.

[14] M.-O. Coppens, Y. Cheng, C.M. Van den Bleek. Controlling fluidized bed operation using a novel hierarchical gas injection system. Paper presented at: AIChE Annual Meeting; 1999; Dallas, USA.

[15] M.-O. Coppens. Geometrical control of multiphase processes using a new fluid injection system. Paper presented at: AIChE Annual Meeting; 1999; Dallas, USA.

[16] M.-O. Coppens, 2001. Method for operating a chemical and/or physical process by means of a hierarchical fluid injection system. U.S. Patent 6333019.

[17] D. Christensen, J. Nijenhuis, J.R. van Ommen, M.O. Coppens, Influence of distributed secondary gas injection on the performance of a bubbling fluidized-bed reactor, Ind. Eng. Chem. Res. 47 (2008) 3601-3618.

[18] D. Christensen, J. Nijenhuis, J.R. Van Ommen, M.O. Coppens, Residence times in fluidized beds with secondary gas injection, Powder Technol. 180 (2008) 321-331.

[19] M.-O. Coppens, Nature-inspired chemical engineering for process intensification, Annu. Rev. Chem. Biomol. Eng. 12 (2021) 187-215.

[20] K. Adriany, E. Bayat, N. Garrett, R. Pedersen, R. Weekes, A. Tran, 2019. Fractal fluid passages apparatus. U.S. Patent 16/296,101.

[21] S. Wang, X. Sun, C. Xu, J. Bao, C. Peng, Z. Tang, Investigation of a circulating turbulent fluidized bed with a fractal gas distributor by electrostatic-immune electrical capacitance tomography, Powder Technol. 361 (2020) 562-570.

[22] L. Zhao, G. Zeng, Y. Gu, Z. Tang, G. Wang, T. Tang, Y. Shan, Y. Sun, Nature inspired fractal tree-like photobioreactor via 3d printing for co2 capture by microalgae, Chem. Eng. Sci. 193 (2019) 6-14.

[23] L. Wang, W. Wu, X. Li, Numerical and experimental investigation of mixing characteristics in the constructal tree-shaped microchannel, Int. J. Heat Mass Transf. 67 (2013) 1014-1023.

[24] P. Trogadas, M.-O. Coppens, Nature-inspired electrocatalysts and devices for energy conversion, Chem. Soc. Rev. 49 (2020) 3107-3141.

[25] L. Luo, Z. Fan, H. Le Gall, X. Zhou, W. Yuan, Experimental study of constructal distributor for flow equidistribution in a mini crossflow heat exchanger (MCHE), Chem. Eng. Process. 47 (2008) 229-236.

[26] Y. Chen, F. Yao, X. Huang, Mass transfer and reaction in methanol steam reforming reactor with fractal tree-like microchannel network, Int. J. Heat Mass Transf. 87 (2015) 279-283.

[27] D. Gu, M. Ye, X. Wang, Z. Liu, Numerical investigation on mixing characteristics of floating and sinking particles in a stirred tank with fractal impellers, J. Taiwan Inst. Chem. Eng. 116 (2020) 51-61.

[28] S. Jiang, J. Wang, L.-F. Feng, M.-O. Coppens, Fractal injectors to intensify liquid-phase processes by controlling the turbulent flow field, Chem. Eng. Sci. 238 (2021) 116616.

[29] Y. Fan, L. Luo, Recent applications of advances in microchannel heat exchangers and multi-scale design optimization, Heat Transf. Eng. 29 (2008) 461-474.

[30] E. Ivanova, M. Di Domenico, B. Noll, M. Aigner. Unsteady simulations of flow field and scalar mixing in transverse jets. Paper presented at: Proceedings of the ASME Turbo Expo 2009: Power for Land, Sea, and Air. Volume 2: Combustion, Fuels and Emissions; 2009; Orlando, Florida, USA.

[31] Z. Yang, Assessment of unsteady-rans approach against steady-rans approach for predicting twin impinging jets in a cross-flow, Cogent Eng. 1 (2014) 936995.

[32] V. Yakhot, S.A. Orszag, S. Thangam, T.B. Gatski, C.G. Speziale, Development of turbulence models for shear flows by a double expansion technique, Phys. Fluid. Fluid Dynam. 4 (1992) 1510-1520.

[33] R. Gu, K. Cheng, L. Wen, Application of the engulfment model in assessing micromixing time of a micro-impinging stream reactor based on the determination of impinging zone with CFD, Chem. Eng. J. 409 (2021) 128248.

[34] S. Jiang, J. Wang, L.-F. Feng, M.-O. Coppens, Hydrodynamics and local turbulent mixing of submerged, parallel liquid jets: Experiments and CFD simulations, Ind. Eng. Chem. Res. 59 (2020) 3985-3995.

[35] M. Salmhofer, The renormalization group, Renormalization, Springer, Berlin, Heidelberg, 1999, pp. 63-112.

[36] J. Baldyga, J.R. Bourne, Simplification of micromixing calculations. I. Derivation and application of new model, Chem. Eng. J. 42 (1989) 83-92.

[37] J. Baldyga, J.R. Bourne, Simplification of micromixing calculations. Ii. New applications, Chem. Eng. J. 42 (1989) 93-101.

[38] Y. Han, J.-J. Wang, X.-P. Gu, L.-F. Feng, Numerical simulation on micromixing of viscous fluids in a stirred-tank reactor, Chem. Eng. Sci. 74 (2012) 9-17.

[39] B.F. Magnussen, B.H. Hjertager, On mathematical modeling of turbulent combustion with special emphasis on soot formation and combustion, Symp. Combust. 16 (1977) 719-729.

[40] P. Wang, The model constant a of the eddy dissipation model, Prog. Comput. Fluid Dyn. 16 (2016) 118-125.

[41] Y. Ouyang, Y. Xiang, H. Zou, G. Chu, J. Chen, Flow characteristics and micromixing modeling in a microporous tube-in-tube microchannel reactor by CFD, Chem. Eng. J. 321 (2017) 533-545.

[42] W. Li, F. Xia, H. Qin, M. Zhang, W. Li, J. Zhang, Numerical and experimental investigations of micromixing performance and efficiency in a pore-array intensified tube-in-tube microchannel reactor, Chem. Eng. J. 370 (2019) 1350-1365.

[43] M.C. Fournier, L. Falk, J. Villermaux, A new parallel competing reaction system for assessing micromixing efficiency—determination of micromixing time by a simple mixing model, Chem. Eng. Sci. 51 (1996) 5187-5192.

[44] M.C. Fournier, L. Falk, J. Villermaux, A new parallel competing reaction system for assessing micromixing efficiency—experimental approach, Chem. Eng. Sci. 51 (1996) 5053-5064.

[45] P. Guichardon, L. Falk, M. Andrieu, Experimental comparison of the iodide-iodate and the diazo coupling micromixing test reactions in stirred reactors, Chem. Eng. Res. Des. 79 (2001) 906-914.

[46] P. Guichardon, L. Falk, Characterisation of micromixing efficiency by the iodide–iodate reaction system. Part i: Experimental procedure, Chem. Eng. Sci. 55 (2000) 4233-4243.

[47] T. Lemenand, D. Della Valle, C. Habchi, H. Peerhossaini, Micro-mixing measurement by chemical probe in homogeneous and isotropic turbulence, Chem. Eng. J. 314 (2017) 453-465.

[48] C. Habchi, T. Lemenand, D.D. Valle, H. Peerhossaini, Turbulent mixing and residence time distribution in novel multifunctional heat exchangers–reactors, Chem. Eng. Process. 49 (2010) 1066-1075.

[49] J. Jeong, F. Hussain, On the identification of a vortex, J. Fluid Mech. 285 (1995) 69-94.

[50] S. Jayanti, Hydrodynamics of jet mixing in vessels, Chem. Eng. Sci. 56 (2001) 193-210.

[51] A. Durve, A.W. Patwardhan, I. Banarjee, G. Padmakumar, G. Vaidyanathan, Numerical investigation of mixing in parallel jets, Nucl. Eng. Des. 242 (2012) 78-90.

Graphical abstract

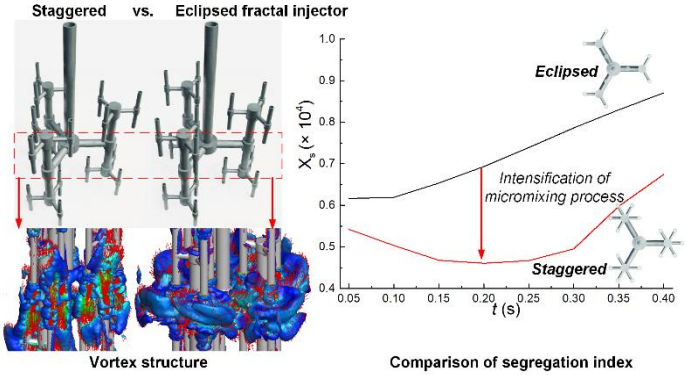

Vortex structure

Comparison of segregation index